



Performance characteristics of lithium coin cells for use in wireless sensing systems: Transient behavior during pulse discharge

Yin Zhang, John N. Harb*

Department of Chemical Engineering, Provo, Brigham Young University, UT 84602, USA

HIGHLIGHTS

- The pulse discharge behavior of lithium coin cells is examined.
- An analytical model of battery behavior is developed.
- Critical factors are identified for battery-aware design of wireless sensors.

ARTICLE INFO

Article history:

Received 21 August 2012

Received in revised form

17 November 2012

Accepted 21 November 2012

Available online 12 December 2012

Keywords:

Lithium coin cell

Pulse discharge

Wireless sensor power

Battery-aware design

ABSTRACT

An understanding of the pulse discharge behavior of commercial lithium coin cells in wireless sensing systems (WSs) is critical to prolonging the operating life and/or reducing the size of such systems. This paper is part of an effort to examine, model and optimize battery performance for sensor duty cycles consisting of multiple pulse discharges. The transient behavior of the cells during pulse discharge and the relaxation behavior following the pulse are both investigated with single-pulse experiments, and described with a simple mathematical model. In both cases, the voltage response is characterized by a region of rapid change, associated with ohmic and interfacial resistances, followed by a region of slower change. Solid phase diffusion in the cathode is the major contributor to the “slow” voltage change that occurs during and after a pulse. A simple analytical model, validated for this system, was found to accurately describe the time-dependent voltage and the corresponding non-uniform concentration distribution for the porous electrode. This transient study provides insight into and a description of the factors that influence and control battery behavior during pulsed cycling, and provides a tool to enable the next generation of battery-aware design of autonomous wireless sensing systems.

© 2012 Elsevier B.V. All rights reserved.

1. Introduction

The reduction in size and power consumption of electronic devices has enabled the development of small autonomous systems for sensing and communication [1]. In contrast to the considerable progress made in wireless sensor (WS) and wireless sensor network (WSN) technology over the last decade, the ability to provide power to these sensors remains a challenge. Most currently available wireless sensors require batteries as the energy source [2]. However, the desired small form factor for the system often prohibits the use of large capacity batteries. Additionally, in some applications, replacement of on-board batteries can be cost prohibitive, or even impossible, once the sensors are deployed. Consequently, energy efficiency is of utmost importance in WSN design. There is also a growing awareness that WS operating conditions or duty cycles

can greatly impact the amount of deliverable energy available from a battery [3–5]. The investigation and characterization of performance limitations and tradeoffs related to the use of batteries in WSs are of great interest to those developing wireless sensing systems and networks. A more complete understanding of the influence of WS operating conditions on battery performance and lifetime is critical to our ability to maximize the energy that can be extracted from a given battery in order to prolong the operating life and/or reduce the size of battery-powered WSs.

Lithium or lithium-ion batteries represent an attractive option for use in wireless sensors due to their high operating voltage and high energy density. Small lithium batteries, either replaceable (primary) or rechargeable (secondary), are commercially available as coin type cells, whose diameters range from less than 5 mm to 2–3 cm [6–8]. A number of lithium coin battery chemistries have been developed to meet various application requirements and voltage levels. These include the CR (primary) and ML (secondary) series, which use manganese oxide-based cathodes and a lithium–aluminum alloy anode. For the MT series, lithium titanium oxide is

* Corresponding author. Tel.: +1 801 422 4393; fax: +1 801 422 0215.

E-mail address: john_harb@byu.edu (J.N. Harb).

used for the anode to produce a cell with a nominal voltage of 1.5 V, suitable for direct use in a number of consumer applications. Commercial lithium coin cells, in general, are designed to maximize energy density, and are most suitable for low-rate current drain (3–100 μ A) applications such as memory backup.

The average power required for wireless sensors is frequently low, since many of the sensors operate on an intermittent duty cycle in order to minimize energy consumption [9–12]. Duty cycles commonly seen with WSNs consist of very short (tens to hundreds of milliseconds) pulses of mA magnitude separated by much longer “standby” periods where little or no power is required. The resulting average power (on the order of a few to hundreds of microwatt) can be easily met by lithium coin cells. However, the high power pulses must also be supplied in order to enable functions such as RF transmission and reception. In many cases, the maximum or peak current is many times greater than the standby current, often differing by orders of magnitude. The pulse power capability of lithium coin cells must be understood and characterized in order to most effectively use these cells in power systems for WSNs. Specifically, an understanding of the transient response of the batteries to intermittent current pulses and a description of the physical processes that determine that response are needed in order to predict battery performance and optimize battery life for WSN applications.

In this study we investigate battery discharge characteristics under WSN operating conditions, and demonstrate the suitability of small-sized commercial lithium coin cells for sensor duty cycles. This paper is focused on electrochemical analysis of the transient pulse discharge and the subsequent relaxation processes that take place in the battery in order to provide a basis for understanding and optimizing battery performance for sensing duty cycles. A quantitative mathematical description of the observed battery behavior is provided as part of the analysis. This work with ML1220 cells demonstrates how a physical understanding of battery operation can be developed and put into a form that is usable for WSN system design and optimization. Therefore, the applicability of the approach and results provided in this work extend well beyond the specific cells and chemistries considered.

2. Experimental

The most common rechargeable lithium coin cells on the market are MnO_2/LiAl (ML) and $\text{V}_2\text{O}_5/\text{LiAl}$ (VL) cells. The ML cells typically have a higher energy density than the VL cells (e.g. the nominal capacity of ML1220 is 17 mAh compared to 7 mAh of VL1220). ML1220 cells (Panasonic) were chosen for use in this study as the ML1220 is the smallest cell in ML series that is able to provide the 10–20 mA pulse current needed for many WSNs [10,11]. The diameter and height of these cells, including the case, are 12.5 mm and 2 mm respectively. The cathode disk inside the case has a diameter of ~ 7.6 mm and thickness of ~ 1.0 mm. The ML series cells use a composite manganese oxide for the cathode [13], and a lithium–aluminum alloy for the anode [14]. The electrolyte consists of a lithium-ion conducting salt solvated in ethylene carbonate, butylene carbonate and dimethyl carbonate [15]. The rated capacity at 30 μ A between 2.0 V and 3.1 V is 17 mAh. The 2.0–3.1 V range is recommended by the manufacturer to ensure a long cycle life, and was adopted for this study.

The open circuit voltage of ML1220 cells as shipped is about 2.7 V. The cells were first discharged to 2.0 V at 0.05 mA, and then charged to 3.1 V before testing. Battery charging was performed at a constant current of 1 mA to a maximum voltage of 3.1 V, followed by charging at a constant voltage of 3.1 V until the current dropped below 5 μ A. Pulse cycling tests and transient pulse-relaxation tests were performed with a Maccor 4300 battery testing system.

Electrochemical impedance spectroscopy (EIS) tests were performed using a frequency response analyzer (Gamry Instruments, PC4-750, EIS 300) over a frequency range of 100 kHz–0.1 Hz. EIS experiments utilized the galvanostatic mode of the instrument, where a small sinusoidal current was applied to the cell and the response of the voltage was measured. The EIS experiments were carried out on fully charged cells that had been allowed to relax at open circuit for 5 h following charging. All tests were carried out at room temperature.

3. Results and discussion

The battery capacity during continuous, constant current discharge was evaluated for a range of currents between 0.03 and 50 mA (Fig. 1). At low rates (30–50 μ A), the observed capacity was essentially the rated capacity of 17 mAh. At moderate to high rates, the capacity decreased significantly with increasing discharge current. The inset shows the battery performance at higher currents (10–50 mA), corresponding to C-rates of 0.6–3.0 C. At 10 mA, the discharge time was 275 s and the capacity obtained was 0.76 mAh, about 4.5% of the full capacity. At 20 mA, the battery discharged for ~ 30 s before the cut-off voltage was reached, and the capacity achieved was less than 0.2 mAh. When the current was higher than 30 mA, the battery reached 2.0 V in less than 3 s, reflecting little usable capacity at that rate. Although 20 mA is only equivalent to a 1.2 C-rate for the battery, it corresponds to a current density of 44 mA cm^{-2} based on the geometric area of the cathode disk. When the entire cross-sectional area of the coin cell is considered (including the case), the cell delivered ~ 40 mW cm^{-2} at 20 mA, and 1.2 J cm^{-2} out of the 125 J cm^{-2} total energy available was obtained before the cut-off voltage was reached.

When the battery was pulse discharged (10 mA, 0.1 s pulses and 25 μ A, 2 s standby), a recovery of the battery voltage was observed during the standby period. This resulted in a significant increase in capacity relative to a constant current discharge at the same 10 mA rate, as shown in Fig. 2. An example of the detailed current and voltage profiles for this duty cycle is shown in Fig. 3. Data were collected every 200 cycles, and data for 3 sequential cycles were recorded each time. Fig. 2 shows a total of 201 recordings that appear as 201 pulses, as the 3 sequential cycles overlap on this scale. A total of 40,200 pulses were obtained before the voltage dropped to 2.0 V. The overall capacity of the battery operating under the pulse duty cycle was 11.7 mAh, 95% of which was delivered at the 10 mA peak current. This capacity was about 70% of the full capacity of the cell, and was 15 times higher than the

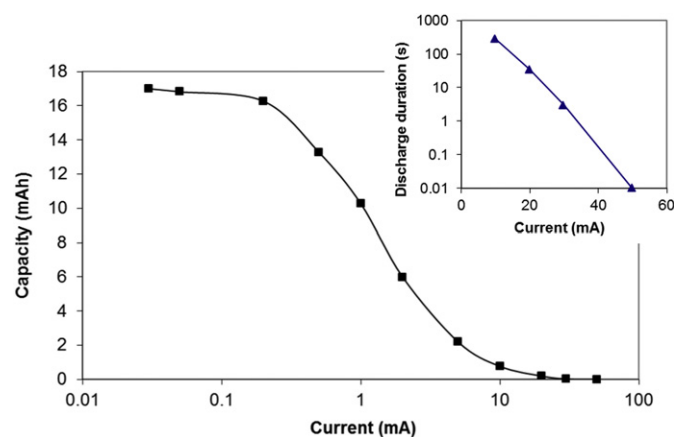


Fig. 1. Performance of ML1220 cells during galvanostatic discharge at different rates.

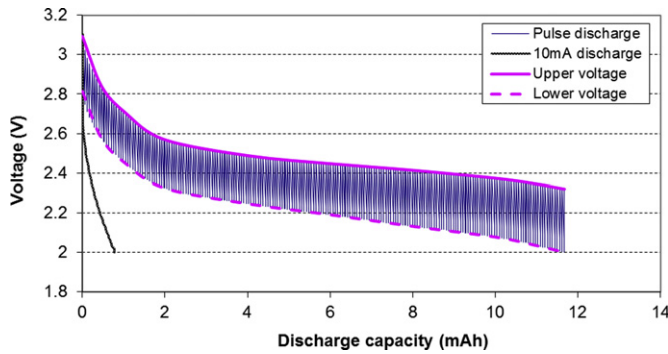


Fig. 2. Pulse discharge of an ML1220 cell using a duty cycle with 10 mA, 0.1 s pulses and a 25 μ A, 2 s standby between pulses.

capacity obtained from a continuous discharge at 10 mA. The peak power delivered was 20–28 mW as the voltage decreased along the discharge, which was sufficient to provide the active power needed for microsensors and low-power WSs.

During pulse discharge of the battery, the operating voltage varied between an upper and a lower voltage, as shown in Figs. 2 and 3, where the upper voltage was the highest voltage reached during standby (point B in Fig. 3) and the lower voltage was the lowest voltage during a pulse (point A). The operating voltage plays a key role in determining battery lifetime and power in wireless sensing systems. The full discharge capacity for the battery under a given duty cycle is assumed to be reached when the battery voltage drops below the lower limit specified for the cell. For a WS system, this limit will be reached during a discharge pulse where point A in Fig. 3 drops below the cut-off voltage. The upper and lower voltages of the pulse discharge depend on losses associated with the various electrochemical processes taking place in the cell.

Important aspects of this study include identification of the dominant electrochemical processes that control the behavior of the battery, and the development of a theoretical description of those processes that includes the time-dependent cell voltage observed during pulse discharge. The need for this information is evident from the results shown in Fig. 2, where use of pulse discharges with intermediate relaxation increased the capacity of the battery by a factor of 15 over the capacity observed at the same rate under constant discharge conditions. An understanding and

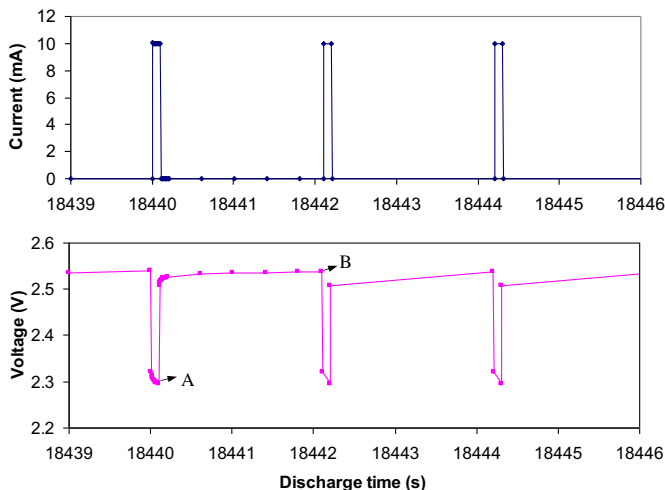


Fig. 3. Current and voltage profiles of the 8801th–8803th cycles extracted from the pulse discharge data described in Fig. 2.

quantitative description of battery behavior during WS duty cycles will provide a basis for optimizing battery and system performance and lifetime.

3.1. Transient analysis of single-pulse discharge

Fig. 4(a) shows voltage vs. time data for 5 mA, 10 mA and 20 mA pulses of 400 ms duration that were initiated from an initial open circuit potential (OCP) of 3.1 V. Data were recorded every 10 ms during the first second following initiation of the pulse, and then at longer time intervals (0.1 s) for the balance of the relaxation period. The voltage profiles, both during and after the pulse, had two parts: a region of rapid voltage change and a region of slower change, as illustrated in Fig. 4(b). When the current was applied, there was an immediate voltage drop, $dV1$, which was estimated as the difference between the open circuit voltage before the pulse and the voltage at the first measurement point ($t = 10$ ms). As time increased, the cell voltage continued to decrease due to the mass transport processes in the battery. The voltage change, $dV2(t)$, is measured relative to the voltage at 10 ms. In Fig. 4(b), $dV2$ shows the voltage change from $t = 10$ ms to $t = 400$ ms, i.e. $dV2(400$ ms). After the current was interrupted at the end of the pulse, an immediate voltage rise was observed. This voltage change, labeled as $dV3$, is defined as the difference between the end of discharge voltage at 400 ms and the voltage corresponding to the first data point of relaxation at 410 ms. Following this immediate voltage jump, there was a slower period of relaxation until the voltage remained constant at the open circuit value (relaxation at longer times not shown in the figure). This voltage change, $dV4(t)$, was defined as the difference between the voltage measured at time t during relaxation (after completion of the pulse) and the final value at or near the open circuit voltage of the battery. In Fig. 4(b), $dV4$ shows the voltage change at $t = 410$ ms, i.e. $dV4(410$ ms). Because the pulse duration was very short, the change in the state-of-charge of the battery was not significant. For example, a 400 ms, 20 mA pulse discharge consumed a capacity of 0.002 mAh, which changed

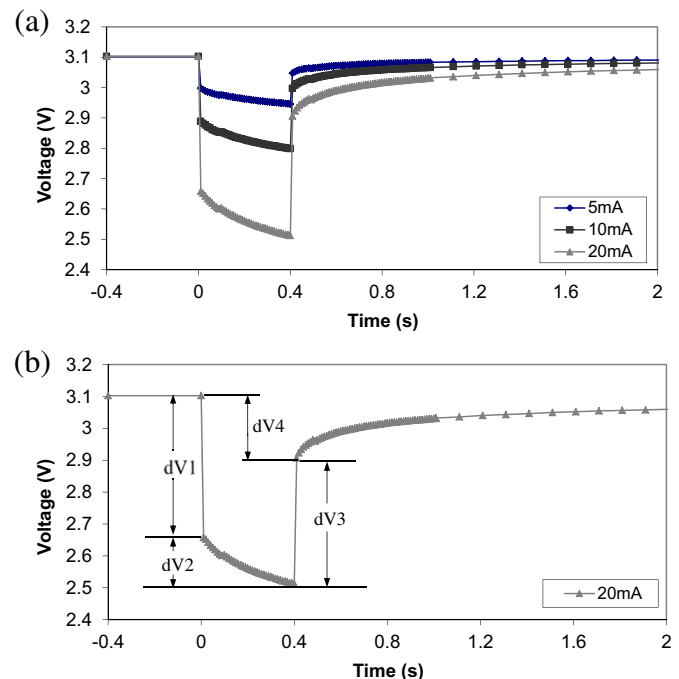


Fig. 4. (a) Voltage response to 5 mA, 10 mA and 20 mA pulses of 400 ms duration; (b) Voltage change illustration labeled for the 20 mA pulse curve.

the battery state-of-charge by only 0.013%. For this reason, the equilibrium potential of the battery was considered to be the same before and after the pulse discharge.

In order to examine the processes important to the short time scales of interest, electrochemical impedance spectroscopy (EIS) was performed on fully charged ML1220 cells. Fig. 5 shows the Nyquist plots for a frequency range of (0.1–100 kHz). The intercept of the semicircle and the Z real axis at high frequencies (~ 100 kHz) yielded a value of $\sim 13 \Omega$ for the battery, which includes both ionic and electronic resistances. These resistances are characterized by a linear relationship between current and voltage, and dominate the behavior at high frequencies where other resistances are not important. IR losses/recovery constitute a significant portion of the rapid voltage changes dV1 and dV3 shown in Fig. 4(b).

The complex impedance in the mid-frequency range (250–60 kHz) includes the influence of both the double layer capacitance and the charge-transfer resistance of the battery [16]. The charge-transfer resistance was estimated as $\sim 7 \Omega$ from the diameter of the depressed semicircle as described by Bard and Faulkner [17]. The time constant for double layer charging was estimated from the frequency (~ 2500 Hz) at the top of the semicircle as ~ 0.5 ms [17]. Because this time is short relative to the times of interest to the current study, double layer charging was not included in our transient modeling. The approximately linear portion of the Nyquist plot at low frequencies (0.1–250 Hz) is associated with diffusion effects in both the electrolyte and the solid phase active material.

In Fig. 5, EIS experiments were carried out at an RMS current amplitude of 25 μ A, as well as at a much higher value of 20 mA. The variation of impedance with the amplitude of the sinusoidal current can be used to investigate the kinetic behavior of the battery [18]. If the relationship between current and surface overpotential is exponential, as is frequently the case, the observed kinetic impedance should decrease as the current increases. In contrast, when the current varies linearly with the surface overpotential, the resulting impedance will not depend on the amplitude of the applied sinusoidal current. As seen in Fig. 5, the 20 mA and 25 μ A curves are essentially the same, indicating pseudo-linear kinetics over the current range used in our studies.

The rapid voltage change (dV1 and dV3 in Fig. 4) that occurred at the beginning and ending of each pulse was further analyzed and plotted against the applied current in Fig. 6. This rapid voltage change was caused by the total of IR resistance and kinetic resistance of the cell. From the EIS results, the ohmic and kinetic resistances were estimated as 13Ω and 7Ω respectively. The total resistance added up to $\sim 20 \Omega$, which at 5, 10 and 20 mA should

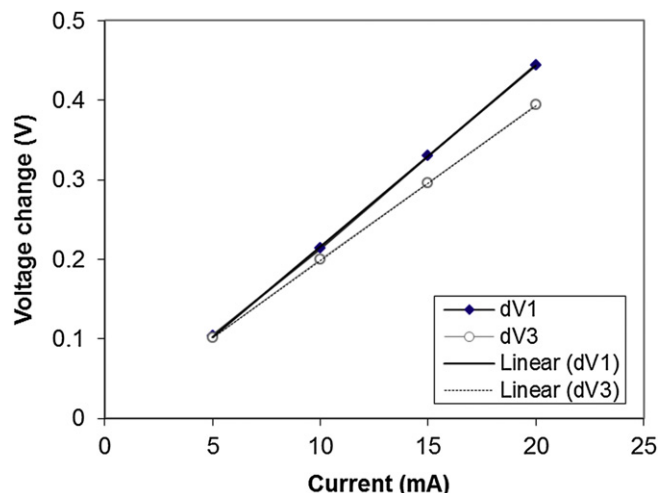


Fig. 6. The rapid voltage change during (dV1) and after (dV3) current pulses of different magnitude.

cause a voltage drop of 0.1, 0.2 and 0.4 V respectively. These values compare reasonably well with the observed voltage changes shown in Fig. 6. Both dV1 and dV3 were linearly proportional to the applied pulse current, consistent with the pseudo-linear kinetics described above. The fast voltage change after the pulse (dV3) is a rapid relaxation of the overpotentials associated with dV1, and should be similar in magnitude to dV1. The difference between dV1 and dV3 at the same current is likely due to local composition changes.

While the rapid voltage change dV1 was a function of only the pulse current, the slower voltage change dV2 during the pulse depended on both current and time. When dV2 in Fig. 4 was plotted against the square root of the time, a linear relationship was immediately apparent (see Fig. 7). The slightly irregular voltages between 0.25 and 0.3 $s^{1/2}$ are an artifact caused by the testing system software around $t = 60$ – 90 ms due to a time step adjustment during data collection. Because dV2 was calculated relative to the voltage at 0.01 s, dV2 was zero at $t = 0.1 s^{1/2}$ for all currents. This, of course, is an approximation as the effects related to composition change begin immediately. The intercepts extrapolated from the linear correlations to $t = 0$ are related to the voltage changes that took place in the first 0.01 s. The square root of time

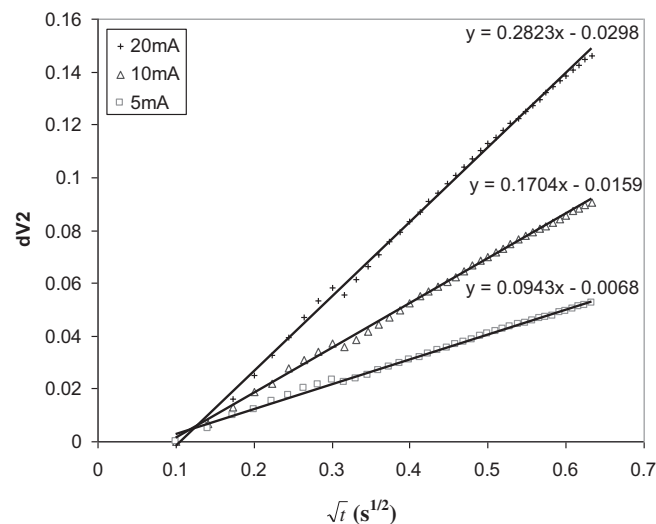


Fig. 7. The voltage change as a function of the square root of time during 400 ms discharge pulses at currents of 5, 10 and 20 mA.

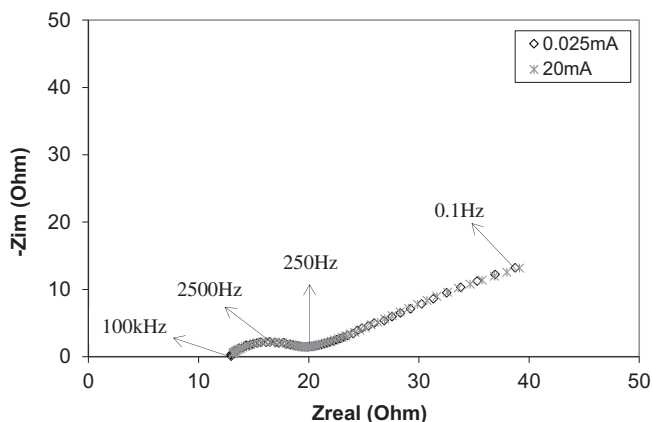


Fig. 5. Nyquist plot for a fully charged ML1220 cell at open circuit (OCV = 3.1 V) for two different amplitudes of the applied sinusoidal current.

dependence is characteristic of that observed for the concentration during transient diffusion, which may be important in this system. The slopes of the curves increased with current (for a constant pulse width of 400 ms), with the magnitude of the slope roughly proportional to the current.

A similar linear relationship between the voltage and the square root of time was observed by Weppner and Huggins [19], who applied a galvanostatic intermittent titration technique (GITT) to a Li_3Sb electrode. Their experiments, performed on dense planar electrodes, showed a linear relationship between voltage and solid phase concentration over a limited range of SOC, and voltage/time behavior that was controlled by diffusion in the solid phase. The applicability of these conditions to the cells of interest to the present study is examined below. In doing this we note that, in contrast to the planar electrodes used by Weppner and Huggins, the ML1220 cells have a thick porous cathode, and application of their analysis to the present study requires a knowledge of the current distribution in the porous electrode.

As we seek a quantitative description of the slow transitions that take place during pulse discharge and relaxation (see Fig. 4), an understanding of the physical processes that control cell performance is critical. In ML1220 cells, the cathode layer (1 mm) is much thicker than the separator (50–100 μm) and the LiAl anode layer (100–200 μm). The lithium diffusion coefficient of the LiAl alloy was found to be on the order of $10^{-6} \text{ cm}^2 \text{ s}^{-1}$ at 415 $^\circ\text{C}$ [20] and $10^{-9} \text{ cm}^2 \text{ s}^{-1}$ at room temperature [21], which is significantly higher than that of the manganese oxide material used in the cathode. For lithiated manganese dioxide ($\text{Li}_{0.33}\text{MnO}_2$), the reported diffusion coefficient ranged from 3×10^{-12} to $6 \times 10^{-11} \text{ cm}^2 \text{ s}^{-1}$ [22]. Moreover, the LiAl alloy anode is typically cycled across a two-phase ($\alpha + \beta$) region, within which the voltage of the LiAl electrode remains constant during lithium insertion and extraction [23]. Therefore, it is unlikely that the slow changes in voltage observed during pulse discharge are due to the anode. It is hence reasonable to expect that the transport processes in the cathode dominate the transient voltage change during the pulse.

As we examine transient transport in the cathode, we first consider the role of liquid phase transport. At room temperature, the diffusion coefficient of the electrolyte is generally in the range of 2×10^{-6} – $4 \times 10^{-6} \text{ cm}^2 \text{ s}^{-1}$ depending on the lithium-ion concentration [24]. Since the detailed composition and properties of the electrolyte are unknown, we assume a diffusivity value on the lower end, $2 \times 10^{-6} \text{ cm}^2 \text{ s}^{-1}$, for calculation purposes. If the Li concentration is 1 M, and the porosity of the cathode layer is 0.4, the total amount of Li^+ in the liquid phase of the cathode is $\sim 1.8 \times 10^{-5} \text{ mol}$. A 20 mA 0.4 s pulse consumes $\sim 8.3 \times 10^{-8} \text{ mol}$ of Li^+ in the cathode and releases the same amount of Li^+ to the electrolyte in the anode. This should cause little change to the bulk concentration of the electrolyte in the cathode. The Li-ion concentration at the electrode surface may vary somewhat from that of the bulk, but the associated overpotential is not expected to be large due to the large interfacial area of the porous electrode and the short discharge time. Indeed, an estimate of the concentration overpotential associated with differences in the concentration between the particle surface and the bulk of the pore was only 0.2 mV. Consequently, it appears that the solid phase mass transfer in the cathode is the dominant contributor to the voltage change during the pulse.

To gain insight into the current distribution across the cathode, the dimensionless exchange current [25] is considered for linear or pseudo-linear kinetics:

$$\nu^2 = (\alpha_a + \alpha_c) \frac{F a i_0 L^2}{RT} \left(\frac{1}{\kappa^{\text{eff}}} + \frac{1}{\sigma^{\text{eff}}} \right) \quad (1)$$

where L is the thickness of the electrode. If ν^2 is large, the reaction distribution in the electrode is non-uniform. The penetration depth, within which reaction rates are appreciable, can be estimated by L/ν where α_a and α_c are the apparent transfer coefficients, (often taken to be 0.5 for lithium batteries), F is Faraday's constant, R is the ideal gas constant and T is temperature (298 K for this study). Physical parameters include: a , the specific surface area per volume; κ^{eff} , the effective conductivity of the electrolyte; σ^{eff} the effective electronic conductivity of the matrix; and i_0 , the exchange current density.

For initial calculations, the particle size ($R_p = 3 \mu\text{m}$) and cathode porosity ($\varepsilon = 0.4$) were estimated from SEM images of the cathode. The dependence of the results on these values will be shown later. The specific surface area can be estimated from R_p and ε for spherical particles by

$$a = \frac{3(1 - \varepsilon)}{R_p} \quad (2)$$

To obtain the electronic conductivity of the cathode layer, the cathode was removed from the battery, washed in a diethyl carbonate solvent, and dried in a glovebox. The conductivity was then measured with use of a four line probe [26], which is similar to a four point probe, under a pressure of $\sim 80 \text{ kPa}$. The four line probe configuration minimized the influence of contact resistance, and consistent conductivity measurements were obtained. The measured value of $0.52 \pm 0.04 \text{ S cm}^{-1}$ represents the effective conductivity σ^{eff} of the cathode matrix consisting of conductive additives, active material, and polymer binder, and is similar to the effective conductivity measured by others for Li-ion cathodes [27]. The ionic conductivity of the electrolyte is about 0.01 S cm^{-1} at room temperature, based on a solution of 1 M LiPF_6 in carbonate solvent mixtures [24]. The effective conductivity of the electrolyte, κ^{eff} , is the bulk conductivity corrected by volume fraction of the liquid phase in the cathode as follows [28],

$$\kappa^{\text{eff}} = \kappa \varepsilon^{1.5} \quad (3)$$

This value is always less than the intrinsic value since $\varepsilon < 1$. The value of $\kappa^{\text{eff}}/\sigma^{\text{eff}}$ is therefore less than 0.01/0.52 or 0.019. Small values of $\kappa^{\text{eff}}/\sigma^{\text{eff}}$ indicate that the reaction occurs preferentially near the electrode–solution boundary close to the separator region [25].

The exchange current density can be inferred from the following relationship for linear or pseudo-linear kinetics [28]:

$$i = i_0 \frac{(\alpha_a + \alpha_c)F}{RT} \eta_s \quad (4)$$

Eq. (4) can be rewritten as:

$$i_0 = \frac{RT}{(\alpha_a + \alpha_c)F \eta_s} \frac{1}{i} = \frac{RT}{(\alpha_a + \alpha_c)F R_{ct}} \frac{1}{i} \quad (5)$$

Since the LiAl anode is known to have higher exchange current densities [29,30], the kinetic resistance obtained from the EIS result in Fig. 5 was due principally to the reaction at the cathode. R_{ct} was estimated to be $3 \Omega\text{-cm}^2$ based on the cross-sectional area of the cathode disk, and the superficial i_0 based on this area was calculated as 8.0 mA cm^{-2} . The actual interfacial area for reaction was estimated as $a \cdot SL/\nu$, where S is the cross-sectional area of the cathode. The penetration depth L/ν was assumed to be the same for short current pulses and for high frequency AC experiments. If R_{ct} is expressed in terms of $a \cdot SL/\nu$, [Eqs. (1) and (5)] can be solved simultaneously by iteration to yield a ν^2 value of 188. The resulting penetration depth, L/ν , was $73 \mu\text{m}$, much less than the electrode

thickness of 1 mm. Thus, the reaction takes place preferentially at the separator–electrode interface in a region of $\sim 70 \mu\text{m}$.

During a short discharge pulse, diffusion in the solid phase can be approximated as a 1-D planar system, since solid diffusion only reaches a very thin layer on the surface of the active particle (diffusion length $2Dt$ is $0.04 \mu\text{m}$ when $t = 0.4 \text{ s}$, $D = 10^{-11} \text{ cm}^2 \text{ s}^{-1}$). The governing equation for transient mass transfer under these conditions is Fick's second law,

$$\frac{\partial c}{\partial t} = D \frac{\partial^2 c}{\partial x^2} \quad (6)$$

The initial and boundary conditions are

$$c = c_0 \quad \text{for } t = 0; \quad (7)$$

$$-D \frac{\partial c}{\partial x} \Big|_{x=0} = \frac{i}{F} \quad \text{for } t > 0; \quad (8)$$

$$c(\infty, t) = c_0 \quad \text{for } t \geq 0. \quad (9)$$

with $x = 0$ at the surface and $x = R_p$ at the center of the active particle. D is the solid phase diffusion coefficient, and i and c_0 are current density and initial concentration, respectively. We assume that the reaction distribution is uniform inside the reaction zone. The local current density i can then be calculated based on the interfacial area $a \cdot SL/\nu$. For short times when $t \ll R_p^2/D$, the solution of Eq. (6) under conditions (7)–(9) can be approximated as

$$c(x = 0, t) = c_0 + \frac{2i\sqrt{t}}{F\sqrt{\pi D}} \quad (10)$$

The change in the cell voltage can be related to the change in the solid surface concentration in Eq. (10) by thermodynamics, i.e. the coulometric titration curve of the active material. The result is an equation that describes the time dependence of the voltage in terms of the electrochemical and material properties of the lithium intercalation material [19]:

$$\frac{dE}{d\sqrt{t}} = \frac{2V_m i}{\sqrt{\pi D F}} \frac{dE}{dy} \quad (11)$$

where V_m is the material molar volume and dE/dy is the slope of the voltage vs. composition curve of the active material. The change in V_m , D and dE/dy with composition can be neglected for a short pulse, so dE/dt should be linear with respect to the current density i , consistent with the results shown in Fig. 7. Eq. (11) can be rearranged to calculate the solid diffusion coefficient [19]:

$$D = \frac{4}{\pi} \left(\frac{i \cdot V_m}{F} \right)^2 \left(\frac{dE/dy}{dE/d\sqrt{t}} \right)^2 \quad (12)$$

While our purpose in this paper is to describe the transient behavior of the battery in order to investigate its impact on performance and lifetime in WS applications, comparison of the diffusivity estimated from Eq. (12) with values reported in the literature provides us with a convenient, independent check of the validity of the equations for the system of interest. Here V_m was assumed to be the molar volume of MnO_2 . This is a reasonable approximation, given that the molar mass of Li_yMnO_2 varies little from MnO_2 , and the density of most lithium manganese oxide material (e.g. $\text{Li}_y\text{Mn}_2\text{O}_4$ [31]) is typically within 20% of that of MnO_2 . The value of dE/dy at 3.1 V was obtained with use of data from Ref. [29], and dE/dt was obtained from Fig. 7 at 5, 10 and 20 mA. With these values the diffusion coefficient D was estimated to be $(3.9 \pm 1.2) \times 10^{-11} \text{ cm}^2 \text{ s}^{-1}$, which was very close to the values reported in Ref. [22]. In contrast, D was incorrectly calculated to be $2.7 \times 10^{-13} \text{ cm}^2 \text{ s}^{-1}$ if a uniform current distribution was assumed for the entire cathode and the total interfacial area was used for current density calculation. These results provide evidence for the validity of the present approach and illustrate the importance of accounting for the non-uniform current distribution in thick electrodes.

The calculations above are based on estimated values of porosity and particle size. The impact of these two parameters was evaluated, and the results are shown in Fig. 8. The results indicate that the penetration depth increases with porosity, but changes little with particle size, and the resulting diffusion coefficient increases with decreasing porosity and increasing particle size. In Eq. (2) the specific area decreases with either increasing porosity or particle size, leading to a decrease in ν . An increase in the porosity also increases the values of κ^{eff} , causing L/ν to increase. The particle radius is varied over a relatively wide range, which causes a significant change in the specific area. The reaction area depends on both specific area and penetration depth. The diffusion coefficient decreases with increasing porosity when the change in L/ν dominates. D varies over an order of magnitude when the particle radius varies from $1 \mu\text{m}$ to $4 \mu\text{m}$, which is driven by the change in the specific area (a). It is clear that the calculated diffusion coefficient is affected by both porosity and particle size. However, the variation caused by uncertainties in these design parameters is small relative to the error that would have resulted from the assumption of a uniform current distribution throughout the entire porous electrode, and can be minimized with improved information regarding the structure and properties of the electrode.

Eq. (11) can be integrated over the pulse length to yield an expression for the voltage change. In Fig. 7, dV_2 was measured relative to the voltage at $t = 10 \text{ ms}$. By including the voltage changes

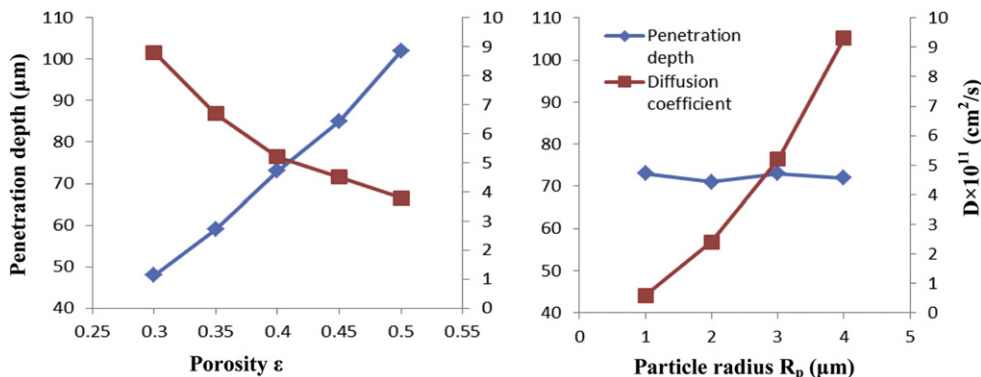


Fig. 8. Influence of porosity and particle size on the penetration depth and solid diffusion.

in the first 10 ms (the y-intercepts), we have the total voltage change during the pulse relative to the voltage at $t = 0$ as:

$$\Delta V_p = F1 \cdot \frac{I}{F2} \cdot \sqrt{t} \quad (13)$$

where ΔV_p varies linearly with applied current I and with square root of time, $F1 = (2V_m/\sqrt{\pi D})(1/F)(dE/dy)$, and $F2 = a \cdot S(L/v)$. The parameter $F1$ is a function of the material properties of the battery including the solid diffusion coefficient, molar volume and thermodynamics; $F2$ reflects the influence of battery design parameters like electrode thickness, geometric area, particle size and porosity. For the short pulses used in WSS, $F1$ and $F2$ can be approximated as constants when the battery state-of-charge (SOC) does not change appreciably. When these electrochemical parameters are not available, data from a single short pulse can be used to determine $F1$ and $F2$ from the relationship between the voltage and t (see Fig. 7).

Eq. (13) can be used for quick and easy estimation of the voltage change under various pulse conditions at a given SOC. When combined with the linear relationship between the instant voltage drop $dV1$ and the applied current, the total voltage change for the pulse can be predicted to yield an estimate of the lower voltage. Caution should be paid to both the current and pulse length range where the above linear relations are valid. For a pulse current no greater than 20 mA, the linear dependence of the voltage on the square root of time was found valid for pulse lengths up to 1 s; this time was longer for lower currents (e.g. 2 s for 5 mA). At higher current (e.g. 20 mA), a deviation from the linear dependence of the voltage on the applied current ($\sim 20\%$ lower) was also found, as shown by the slopes in Fig. 7. Possible explanations include a change in the thermodynamic factor over the pertinent stoichiometric range at longer times or at higher currents [19]. In the case of ML1220 cells, the deviation may also be due to the non-uniform reaction distribution inside the reaction zone and the resulting non-uniform local solid surface concentration.

3.2. Transient analysis of relaxation

In the previous section we established solid phase diffusion as the primary factor that controlled the rate of voltage change beyond the initial voltage drop associated with kinetic and ohmic effects. This section focuses on the relaxation behavior after a pulse discharge. As illustrated in Fig. 4, the voltage profile after a pulse consists of an initial rapid change due to immediate relaxation of the voltage losses associated with kinetic and ohmic resistances, followed by a period of slower change that is associated with relaxation of the concentration gradient in the solid phase. The slow concentration relaxation is critical and is likely the reason for the difference between the low capacity observed for constant current discharge and the much higher capacity observed for pulse discharge at the same rate, but with time for relaxation between the intermittent pulses (see Fig. 2). The interaction of duty cycle and relaxation needs to be understood in order to predict the battery performance in WSS. In this section we quantify the relaxation behavior with use of a transient voltage analysis similar to that used in the previous section.

The voltage profile for the relaxation period is shown in Fig. 9 for a variety of different discharge pulses, each with a current between 5 and 20 mA and duration between 100 and 400 ms. The transient voltage change, $dV4(t) = V_{OCp} - V(t)$, is plotted as a function of the inverse square root of time in Figs. 10 and 11. The relaxation time used in Figs. 10 and 11 is defined as zero at the end of the discharge pulse, and increases from that point. In this section we use t for relaxation time, and τ to designate the length of the pulse that

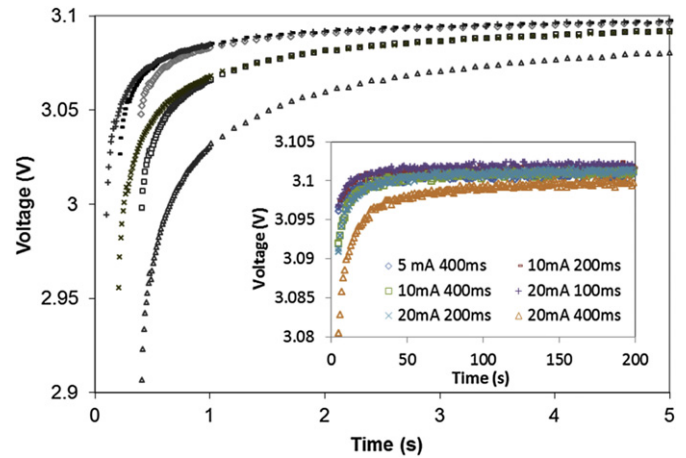


Fig. 9. Voltage relaxation curves following pulses of various currents and lengths. Time is measured from the initiation of the pulse. Inset: relaxation curves for test times from 5 to 200 s.

occurred just previous to the relaxation period of interest. The discontinuity in the voltage curves evident for time axis values of approximately $3.5 \text{ s}^{-1/2}$ is due to an artifact of the measurement system as mentioned above.

The rapid voltage changes $dV1$ and $dV3$ are similar in magnitude, as are $dV4$ at the beginning of the relaxation and $dV2$ at the end of a pulse (i.e., $dV4(t=0) \approx dV2(\tau)$; see Fig. 4). It is apparent from Fig. 9 that the magnitude of the voltage change during relaxation increased with increasing pulse current and length. The rate of change of $dV4$ was greatest at the beginning of the relaxation period, and slowed as the concentration gradient relaxed. $dV4$ varied linearly with $1/t$ at relaxation times greater than $\sim 0.5 \text{ s}$ (i.e., $1/t < 1.4 \text{ s}^{-1/2}$) for all the pulses shown in Figs. 9 and 10. In addition, current pulses of different magnitude and duration approached the same limit if the amount of charge passed during the pulse was the same. For example, in Figs. 9 and 10 we see that the $dV4$ values for the (20 mA, 200 ms) and (10 mA, 400 ms) pulses were very close in magnitude for $1/t < 1.4$. Fig. 11 provides an expanded view of the curves that illustrates the linearity for times greater than 0.5 s; for clarity, the curves that are overlapped with the relaxation voltage for (5 mA, 400 ms) and (10 mA, 400 ms) pulses are not shown in the figure.

The voltage at short times reflected the impact of the local concentration gradient. For example, at $t = 0.01 \text{ s}$ (right axis of the graph), $dV4$ for the (20 mA, 100 ms) pulse was the same as that for the (10 mA, 400 ms) pulse, but later dropped to a lower value due to

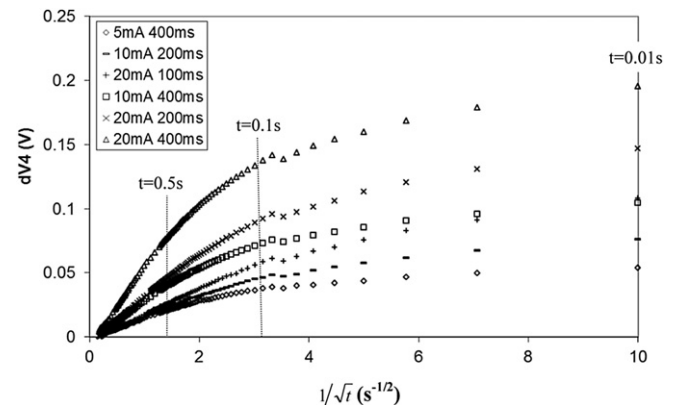


Fig. 10. Transient voltage change versus $1/\sqrt{t}$ during relaxation for $t = 0.01\text{--}30 \text{ s}$.

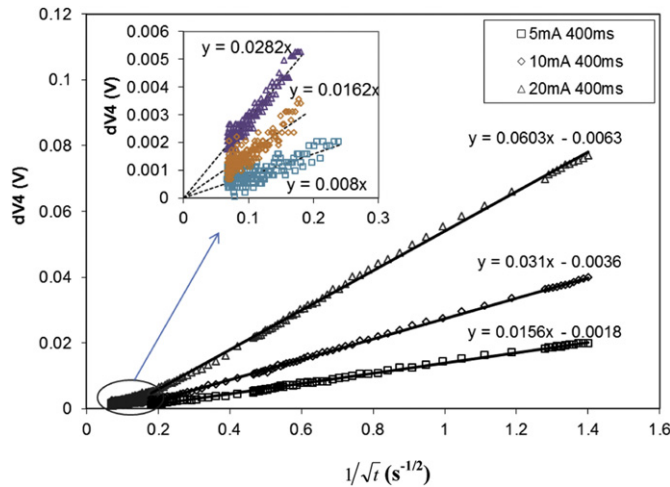


Fig. 11. Transient voltage change versus $1/\sqrt{t}$ during relaxation for $t = 0.5$ – 30 s (inset for $t = 30$ – 200 s).

the lower amount of charge passed during the pulse. The initial value reflected the fact that the surface concentration and local gradient were higher for the higher current pulse, giving a temporarily higher voltage loss that subsequently relaxed to the value expected from the amount of charge passed.

At longer times ($t = 0.5$ – 30 s), the initial concentration distribution in the thin outer layer of the active material particle is of less importance, and diffusion into the bulk of the particle becomes analogous to that of a known quantity of the diffusing species at the surface of the particle that undergoes semi-infinite diffusion. Diffusion in the solid phase can be approximated as a 1-D system because the solid diffusion penetration length ($2Dt = 0.4 \mu\text{m}$ at $t = 30$ s) is small relative to the active particle radius ($3 \mu\text{m}$). The solution for Fick's second law thus can be expressed as [32]:

$$c(x, t) = c_0 + \frac{M}{\sqrt{\pi Dt}} \exp\left(-\frac{x^2}{4Dt}\right) \quad (14)$$

where c_0 is the concentration in the particle prior to the pulse (assumed to be uniform), x is the distance from the surface of the particle, and M is the total amount of material added during the pulse per surface area. M is assumed to be present at the surface of the particle in this calculation and can be calculated from the current density i and the pulse length τ by $M = i\tau/F$. The current density, i , should be based on the actual interfacial area $a \cdot SL/v$, as illustrated in the previous section.

Similar to the derivation of Eqs. (11) and (12), the change of voltage can be related to the change of lithium concentration at the surface of the active particle (at $x = 0$) as follows:

$$\frac{dE}{d(1/\sqrt{t})} = \frac{V_m}{\sqrt{\pi D}} \frac{i \cdot \tau}{F} \frac{dE}{dy} \quad (15)$$

Eq. (15) shows that $dE/d(1/t)$ should vary linearly with the magnitude of the current and the pulse length, consistent with the experimental results shown in Figs. 10 and 11. Note that the voltage change in the region where Eq. (15) is valid depends only on the product of the pulse current and the pulse time, consistent with the overlapping results noted earlier. As expected, and consistent with Eq. (15), the slopes of the lines in Fig. 11 were proportional to the pulse currents at a constant pulse length of 400 ms. With the same physical parameters used in the previous section and the $dE/d(1/t)$ data from Fig. 11 ($t = 0.5$ – 30 s), we used Eq. (15) to estimate the

diffusivity as $D = (4.3 \pm 0.3) \times 10^{-11} \text{ cm}^2 \text{ s}^{-1}$. This value agrees well with the value of $3.9 \times 10^{-11} \text{ cm}^2 \text{ s}^{-1}$ obtained from Eq. (12) using the pulse data instead of the relaxation data used here. The agreement between the diffusivities estimated from the two equations, the linearity of the data with the expected functions of time, the linear dependence of the slopes on the current density for a given pulse length, and the overlap of curves with similar values of $i \cdot \tau$, all confirm the validity of the relationships used to describe voltage changes with time both during the pulse and during relaxation.

At long times (30–200 s), the rate of voltage change became slower than that expected from Eq. (14), as shown in the inset of Fig. 11. The reason for this behavior is likely that the assumption of planar semi-infinite diffusion (Eq. (14)) is no longer valid at long times. Other factors may also contribute, such as the redistribution of lithium from the reaction zone to other areas on the electrode. For practical purposes, the cell voltage was considered to be fully relaxed when it was within 2 mV of the OCV (2 mV is the voltage resolution for the testing system used).

Although over 50% of the overall voltage relaxation took place within the first 0.5 s after the pulse (the “short time” region in Fig. 10 at $1/t > 1.4$), the standby time intervals, within which a WS is most likely to operate, correspond to the linear region shown in Fig. 11 (seconds to minutes). Nearly 80% of the voltage change due to relaxation of current within gradients occurred in the first 2–3 s after the pulse, and only 2–5% of voltage change took place in the long time relaxation region (30 s or longer). Because the establishment of concentration gradients leads to voltage losses, the extent of time available for relaxation may have a significant impact on the available capacity and performance of a battery under WS cycle conditions. In subsequent work, these impacts will be demonstrated experimentally and discussed in the context of the limiting processes identified in this work.

For relaxation in the intermediate linear region, Eq. (15) can be integrated to yield:

$$\Delta V_r = \frac{F1}{2} \frac{I \cdot \tau}{F2} \frac{1}{\sqrt{t}} \quad (16)$$

where ΔV_r is the variation of voltage from the OCV, which varies linearly with the inverse of square root of time, the current I and the length τ of the pulse applied just prior to relaxation. When the y-intercept values in Fig. 11 are small relative to the voltage change of interest, this equation should introduce little error, especially for relaxation times less than 5 s. If greater precision is required, the ΔV_r can be corrected to account for the y-intercept for each current. $F1$ and $F2$ can be obtained from the relaxation data or from the pulse experiments described in the previous section.

Eq. (16) can be used to estimate the length of time required for the voltage to relax to within a certain value (ΔV_r) of the OCV. Once that relaxation time is known for a given cell at a specified temperature, I and τ , it is straightforward to estimate the relaxation time for other pulse currents and lengths. Under these conditions, everything in Eq. (16) is constant except for t , I and τ . Therefore,

$$t \propto I^2 \cdot \tau^2 \quad (17)$$

Eq. (17) can be used to facilitate duty cycle design from a limited amount of experimental data. Of particular interest is the length of time required to approach full relaxation.

4. Conclusion

In this paper, we have examined the transient behavior of a commercial lithium coin cell during pulse discharge and

subsequent relaxation as would occur as part of a sensor duty cycle. A quantitative description of the voltage change with time during the pulse and relaxation is provided as part of the study. With EIS experiments, we identified the magnitude of the rapid voltage losses that occur upon initiation and termination of the pulse that are associated with ohmic and interfacial resistances. The EIS results also indicated a near-linear charge-transfer resistance for the system over the range of currents considered. Solid phase diffusion in the cathode was found to be the major contributor to the “slow” transient voltage change that occurred during and after a pulse. A simple analytical model was developed to describe this time-dependent voltage and the corresponding concentration distribution for a thick porous electrode with a non-uniform current distribution. A fit of the analytical model to experimental data, similar to that shown previously in the literature for planar electrodes, permitted an estimate of the solid phase diffusivity. Independent fitting of the pulse data and relaxation data both yielded a diffusivity of $D \sim 4 \times 10^{-11} \text{ cm}^2 \text{ s}^{-1}$, which agrees well with measured values for this system [22] and provides evidence for the validity of the approach used here to describe the transient behavior of the battery.

The voltage change with time, both during a pulse and following a pulse, were accurately described by the analytical expressions presented in this paper. Thus, this study provides insight into and a description of the factors that influence and control battery behavior during pulsed cycling. Of particular note is the observation that the time required for relaxation is much longer than the pulse length. Consequently, the relaxation time and its relationship to the desired duty cycle will be a critical factor in determining the suitability of a cell for sustained pulse discharge. The quantitative description of the voltage change with time during the pulse and relaxation provides a convenient and powerful tool for predicting cell voltage and a basis for understanding and optimizing battery performance for duty cycles characteristic of wireless sensing systems.

References

- [1] K.D. Wise, *Sensor. Actuat. A: Phys.* 136 (2007) 39–50.
- [2] D. Diamond, S. Coyle, S. Scarmagnani, J. Hayes, *Chem. Rev.* 108 (2008) 652–679.
- [3] C. Park, K. Lahiri, A. Raghunathan, in: *IEEE SECON 2005 Proceedings*, pp. 430–440.
- [4] C. Chau, F. Qin, S. Sayed, M.H. Wahab, Y. Yang, *IEEE J. Selected Areas Commun.* 28 (2010) 1222–1232.
- [5] C.F. Chiasserini, R.R. Rao, in: *Proc. of Mobicom'99, Seattle, 1999*, pp. 88–95.
- [6] <http://www.panasonic.com/industrial/batteries-oem/oem/primary-coin-cylindrical/br-cr.aspx>. (accessed 07.18.12).
- [7] <http://www.panasonic.com/industrial/batteries-oem/oem/rechargeable-coin/index.aspx>. (accessed 07.18.12).
- [8] S. Prakash, W.E. Mustain, P. Kohl, *J. Power Sources* 189 (2009) 1184–1189.
- [9] B.H. Calhoun, D.C. Daly, N. Verma, D.F. Finchelstein, D.D. Wentzloff, A. Wang, S. Cho, A.P. Chandrakasan, *IEEE Trans. Comput.* 54 (2005) 727–740.
- [10] V. Shnayder, M. Hempstead, B. Chen, G.W. Allen, M. Welsh, in: *SenSys '04 Proceedings of the 2nd International Conference on Embedded Networked Sensor Systems*, 2004, pp. 188–200.
- [11] J. Polastre, R. Szewczyk, D. Culler, in: *Fourth International Symposium on IPSN*, 2005, pp. 364–369.
- [12] J.N. Harb, R.M. LaFollette, R.H. Selfridge, L.L. Howell, *J. Power Sources* 104 (2002) 46–51.
- [13] T. Nohma, T. Saito, N. Furukawa, *J. Power Sources* 26 (1989) 389–396.
- [14] T. Nohma, S. Yoshimura, K. Nishio, Y. Yamamoto, S. Fukuoka, M. Hara, *J. Power Sources* 58 (1996) 205–207.
- [15] H. Watanabe, T. Nohma, I. Nakane, S. Yoshimura, K. Nishio, T. Saito, *J. Power Sources* 43–44 (1993) 217–221.
- [16] E. Barsoukov, J.R. Macdonald, *Impedance Spectroscopy, Theory, Experiment, and Applications*, second ed., Wiley, 2005.
- [17] A.J. Bard, L.R. Faulkner, *Electrochemical Methods Fundamentals and Applications*, second ed., Wiley, Hamilton, 2001.
- [18] D. Dees, E. Gunen, D. Abraham, A. Jansen, J. Prakash, *J. Electrochem. Soc.* 152 (2005) A1409–A1417.
- [19] W. Weppner, R.A. Huggins, *J. Electrochem. Soc.* 124 (1977) 1569–1578.
- [20] C.J. Wen, B.A. Boukamp, R.A. Huggins, *J. Electrochem. Soc.* 126 (1979) 2258–2266.
- [21] R.A. Moshtev, P. Zlatilova, B. Puresheva, V. Manev, A. Kozawa, *J. Power Sources* 51 (1994) 409–423.
- [22] C.M. Julien, B. Banov, A. Momchilov, K. Zaghib, *J. Power Sources* 159 (2006) 1365–1369.
- [23] H.J. Bang, S. Kim, J. Prakash, *J. Power Sources* 92 (2001) 45–49.
- [24] L. Valøena, J.N. Reimers, *J. Electrochem. Soc.* 152 (2005) A882–A891.
- [25] J. Newman, K.E. Thomas-Alyea, *Electrochemical Systems*, third ed., Wiley, Hoboken, 2004.
- [26] D.E. Stephenson, *Microstructure and transport properties of porous Li-ion electrodes*, Ph.D. dissertation, Department of Chemical Engineering, Brigham Young University, August 2011.
- [27] Y.-H. Chen, C.-W. Wang, G. Liu, X.-Y. Song, V.S. Battaglia, A.M. Sastry, *J. Electrochem. Soc.* 154 (10) (2007) A978–A986.
- [28] K.E. Thomas, R.M. Darling, J. Newman, *Mathematical Modeling of Lithium Batteries*, Kluwer Academic/Plenum Publishers, 2002.
- [29] T. Ohzuku, M. Kitagawa, T. Hirai, *J. Electrochem. Soc.* 137 (1990) 769–775.
- [30] R. Pollard, J. Newman, *Electrochim. Acta* 25 (1980) 315–321.
- [31] <http://www.inframat.com/products/32B-0825.htm>. (accessed 07.18.12).
- [32] S. Basu, W.L. Worrell, *Fast Ion Transport in Solids*, Elsevier, Amsterdam, 1979, 149–152.